

The peculiar magnetic field morphology of the white dwarf WD 1953-011: evidence for a large-scale magnetic flux tube?

G. Valyavin¹, G.A. Wade², S. Bagnulo³, T. Szeifert⁴, J.D. Landstreet⁵, Inwoo Han¹,
A. Burenkov⁶

ABSTRACT

We present and interpret new spectropolarimetric observations of the magnetic white dwarf WD 1953-011. Circular polarization and intensity spectra of the H α spectral line demonstrate the presence of two-component magnetic field in the photosphere of this star. The geometry consists of a weak, large scale component, and a strong, localized component. Analyzing the rotationally modulated low-field component, we establish a rotation period $P_{rot} = 1.4480 \pm 0.0001$ days. Modeling the measured magnetic observables, we find that the low-field component can be described by the superposition of a dipole and quadrupole. According to the best-fit model, the inclination of the stellar rotation axis with respect to the line of sight is $i \approx 20^\circ$, and the angle between the rotation axis and the dipolar axis is $\beta \approx 10^\circ$. The dipole strength at the pole is about 180 kG, and the quadrupolar strength is about 230 kG. These data suggest a fossil origin of the low-field component. In contrast, the strong-field component exhibits a peculiar, localized structure (“magnetic spot”) that confirms the conclusions of Maxted and co-workers. The mean field modulus of the spot ($|B_{spot}| = 520 \pm 7$ kG) together with its variable longitudinal magnetic field having a maximum of about +400 kG make it difficult to describe it naturally as a high-order component of the star’s global poloidal field. Instead, we suggest that the observed strong-field region has a geometry similar to a magnetic flux tube.

¹Korea Astronomy and Space Science Institute, 61-1, Whaam-Dong, Youseong-Gu, Taejeon, Republic of Korea 305-348

²Physics Department, Royal Military College of Canada, Kingston, Ontario, Canada

³Armagh Observatory, Northern Ireland

⁴European Southern Observatory, Alonso de Córdova 3107, Santiago, Chile

⁵Physics & Astronomy Department, University of Western Ontario, London, Canada

⁶Special Astrophysical Observatory, Russian Academy of Sciences, Nizhnii Arkhyz, Karachai Cherkess Republic, 357147, Russia

Subject headings: stars: individual (WD1953-011 — stars: magnetic fields — stars: white dwarfs

1. Introduction

At present, there are more than one hundred known isolated magnetic white dwarfs (MWDs) with magnetic field strengths from a few tens of kilogauss to several hundreds of megagauss (Angel et al. 1981; Schmidt & Smith 1995; Liebert et al. 2003; Valyavin et al. 2003; Aznar Cuadrado et al. 2004; Valyavin et al. 2006; Kawka et al. 2007; Jordan et al. 2007). It is generally assumed that the magnetic fields of the strong-magnetic MWDs (those with MG-strength fields) are organized as low-order multipolar fields with dominating dipolar components (Putney 1999). The rotation periods and surface magnetic fields of the strong-magnetic MWDs are believed to be stable on long time scales (Schmidt & Northworthy 1991), suggesting that their fields are fossil remnants of the fields of their progenitor stars. A comparison of the field strengths and incidence statistics of the strong-magnetic MWDs with magnetic fields of Ap/Bp main sequence stars support this assumption (Angel et al. 1981).

Despite the progress with the strong-magnetic MWDs, the magnetic properties of the weak-field degenerates are only poorly known. Presently, only a few white dwarfs with kilogauss magnetic fields has been identified (Schmidt & Smith 1995; Fabrika et al. 2003; Valyavin et al. 2003; Aznar Cuadrado et al. 2004; Valyavin et al. 2006; Kawka et al. 2007; Jordan et al. 2007). Their rotation and field geometries are poorly studied, although some progress has been achieved by Maxted et al. (2000) and Wade et al. (2003) with a study of WD 1953-011 and by Valyavin et al. (2005) with WD 0009+501. Maxted et al. (2000) established that the magnetic morphology of WD 1953-011 can be described by both low-field ($B \sim 90$ kG) and strong-field ($B \sim 500$ kG) components. Some evidence for the presence of a non-dipolar (quadrupolar) component was also found in WD 0009+501 by Valyavin et al. (2005).

Motivated by the results of Maxted et al. (2000), we have undertaken collaborative spectropolarimetric monitoring of WD1953-011. In this paper we report results of these observations and analyse them in the manner presented by Wade et al. (2003) and Valyavin et al. (2005). Our goal is to determine precisely the magnetic morphology of this degenerate.

2. A few preliminary remarks

Our preliminary analysis of the spectropolarimetric data obtained with FORS1 at the VLT (Wade et al. 2003) revealed significant variability of the Stokes I and V spectra of WD 1953-011 due to rotation, with a period of about 1.45 days. In Fig. 1 we show those results which illustrate the variation of the Stokes I , V , Q and U profiles of the $H\alpha$ line with rotational phase (phase increases from top to bottom in the figure). As can be seen, the Stokes I profile is strongly variable. The central S-wave of the Stokes V profile is almost constant. However, near rotational phase 0.6 additional broadened Stokes V signatures appear in the $H\alpha$ wings. These signatures correspond to the weak “satellite features” observed by Maxted et al. (2000) in the wings of the $H\alpha$ profile at these phases, and were attributed to the presence of a high-field magnetic structure. Linear polarization Stokes Q and U signatures are only marginally detected at several rotational phases.

In this paper we extend this analysis using additional observational material obtained with the AAT (Maxted et al. 2000) and with the 6-m Russian telescope BTA, and using more sophisticated modeling techniques.

3. Observations

Spectropolarimetric observations of WD 1953–011 were obtained in service mode between May and June 2001 with FORS1 on the ESO VLT. FORS1 is a multi-mode instrument for imaging and multi-object spectroscopy equipped with polarimetric optics, and is described by Appenzeller et al. (1998). For this work, FORS1 was used to measure Stokes $IQUV$ profiles of WD 1953–011 at 12 different rotation phases, using grism 600 R (plus order separation filter GG 435), which covers the interval 5250 Å– 7450 Å. With a slit width of 0.7", the spectral resolving power was about 1650. To perform circular polarization measurements, a $\lambda/4$ retarder waveplate and a Wollaston prism are inserted in the FORS1 optical path (see Appenzeller (1967)). The $\lambda/4$ retarder waveplate can be rotated in 45° steps.

To perform linear polarization measurements, a $\lambda/2$ retarder waveplate is used, which can be rotated in 22.5° steps. At each epoch, Stokes V was measured taking two 420s exposures: one with the $\lambda/4$ retarder waveplate at -45° , and one with the $\lambda/4$ retarder waveplate at $+45^\circ$. Stokes Q and U were measured taking four 600s exposures with the $\lambda/2$ retarder waveplate at 0° , 22.5° , 45° , and 67.5° . The Stokes V/I circular polarization

spectrum was then obtained by calculating

$$P_V = \frac{V}{I} = \frac{1}{2}(r_{-45} - r_{+45}) \quad (1)$$

where

$$r_\alpha = \frac{f^\circ - f^e}{f^\circ + f^e}. \quad (2)$$

In Eq.(2) f° is the flux measured in the ordinary beam and f^e is the flux measured in the extra-ordinary beam, obtained with the $\lambda/4$ retarder waveplate at angle α . Similarly, the linear polarization was obtained by calculating

$$\begin{aligned} P_Q &= \frac{Q}{I} = \frac{1}{2}(r_0 - r_{45}) \\ P_U &= \frac{U}{I} = \frac{1}{2}(r_{22.5} - r_{67.5}) \end{aligned} \quad (3)$$

where r_β is defined by Eq. 2, except that β refers to the position angle of the $\lambda/2$ retarder waveplate. Fluxes f° and f^e were obtained from the raw data after bias correction and wavelength calibrations performed using standard IRAF routines.

These observations were supported by a short observing run at the 6-m Russian telescope BTA where we obtained additional I, V series of spectra of WD 1953-011 using the UAGS spectropolarimeter, with nearly the same resolving power as in the observations with FORS1. The instrument is described in detail by Afanasief et al. (1995) and by Naydenov et al. (2002). The observational technique and data reduction are similar to those described by Bagnulo et al. (2000, 2002) and by Valyavin et al. (2005). A comparative analysis of the spectropolarimetric data obtained from the different telescopes showed identical results. A comparison of the Stokes V spectra obtained with the VLT and BTA is illustrated in Fig. 2. The spectra are obtained at different times but similar rotational phases.

In addition to the spectropolarimetric data from the VLT and BTA, in this paper we also use high-resolution spectroscopic data (Stokes I) obtained at the AAT and described by Maxted et al. (2000). Together with the spectropolarimetry, these data extend the analysis presented by Wade et al. (2003) to a much longer time base. Table 1 gives an overview of all the observations. In the table: **JD** is the Julian Date; **Exp** is an equivalent exposure time of an observation; **Stokes** is the observed Stokes parameter (I, V, Q or U); and **Telescope** is telescope used (VLT, AAT or BTA).

4. Mean field modulus of the magnetic field of WD 1953-011

We begin with an analysis of the low and high-resolution Stokes I spectra, extending over 5 years. These spectra are used for establishing the rotation period of the star, as well as the mean field modulus of the low- and strong-field components.

4.1. The low-field component

The low-field component of WD 1953-011 was first discovered spectroscopically by Koester et al. (1998) and described in detail by Maxted et al. (2000). The mean field modulus, $|B_G|^1$ exhibits a low-amplitude variation due to the star’s rotation, with a period estimated between hours and days (Maxted et al. 2000). These conclusions were made on the basis of the high-resolution spectroscopy of the Zeeman pattern in the $H\alpha$ core.

In our low-resolution FORS1 and BTA observations, Zeeman splitting attributed to the low-field component cannot be resolved spectroscopically. In the spectra the splitting is revealed as an additional variable broadening and desaturation of the $H\alpha$ core. In this case, measurements of the low-field component can be carried out by an analysis of the equivalent widths (EW_{core}) of the $H\alpha$ core. Using field modulus $|B_G|$ values determined by Maxted et al. (2000) from an analysis of individual high-resolution $H\alpha$ line profiles and measuring equivalent widths of the $H\alpha$ cores, we may try to calibrate the relationship $EW_{core} - |B_G|$ to allow us to determine $|B_G|$ in the low-resolution spectra. To obtain the required calibration, we estimated equivalent widths of the $H\alpha$ core from the high resolution spectra obtained by Maxted et al. (2000). In order to work with measurements having a uniform resolution, all high-resolution spectra were convolved with a gaussian instrumental profile to reproduce the spectral resolution of FORS1 and UAGS. The resultant spectra are presented in Fig. 3.

As one can see in Fig. 3, the profiles are strongly variable. The central intensity of the core also correlates with the intensity of the strong-field Zeeman features which are found in the wings of the $H\alpha$ profile (Fig. 3: the two satellite features at $\pm 10 \text{ \AA}$ around the $H\alpha$ core). This correlation (the higher the intensity of the features, the weaker the central intensity) is due to the fact that the spot, which appears periodically on the visible disc due to rotation, redistributes the flux according its projected area. It is also seen that the width of the $H\alpha$ core is variable itself due to the variable Zeeman pattern of the line core. Therefore, to minimize the influence of the variable high-field spectral features in measurements of the central Zeeman pattern attributed to the low-field component, we artificially re-normalized all the profiles to equal residual intensities ($r_c = 0.47$ at the line center) and measured equivalent widths of the central narrow portion ($r_c \leq 0.6$) of the resultant $H\alpha$ profiles. In these conditions, the variation of the $H\alpha$ core is attributed only to the rotationally modulated low-field component. As hoped, we find a close correlation between the EW_{core} measured in this way and the value of $|B_G|$ measured by Maxted. This relation is shown in Fig. 4.

¹For distinctness we label all magnetic observables related to the low-field component with the subscript “G”, assuming its large scale (Global) geometry. Observables related to the strong-field component will be labeled with the subscript “Spot” or “S”.

Finally, using the $|B_G| - EW$ relationship derived from the high-resolution spectra as illustrated in Fig. 4, we inferred the field modulus $|B_G|$ associated with each of the low-resolution spectra (see Table 2).

4.2. The strong-field component

In order to measure the magnetic field modulus $|B_{spot}|$ of the strong-field component we deblended the $H\alpha$ profile by means of a simultaneous fit of five Gaussian profiles (three central profiles used to fit the $H\alpha$ core, and two satellite gaussians to reproduce the strong-field Zeeman pattern). This method enabled us to reproduce the Zeeman splitting of the strong-field component and the corresponding magnetic field strength in those spectra where the strong-field spectral features are seen. The method also allows us to estimate the projected fractional area S of the strong-field area on the disc. Reconstructing by gaussians and extracting the Zeeman pattern of the strong field component from the observed $H\alpha$ line profiles, we determined S , the fraction of the flux absorbed by the strong-field pattern relative to the total $H\alpha$ absorption. The method is rather rough and can be considered as a first-guess approximation that is necessary for the analysis described below. A more realistic calculation of the size of the strong-field area is performed in Sect. 8 where we model the spectra. The results ($|B_{spot}|$ and S) are presented in Table 3. S is given in per cent of the disc area.

5. Mean longitudinal magnetic field of WD1953-011

From the Stokes I and V spectra obtained with the VLT and BTA we determined longitudinal fields through the weak-field approximation (Angel et al. 1973) modified to the analysis of the two-component Stokes V spectra:

$$V(\lambda) \sim (1 - S)B_G^l \left(\frac{\lambda}{\lambda_0}\right)^2 \frac{1}{I(\lambda)} \frac{dI(\lambda)}{d\lambda} + SV(\lambda)_{spot} \quad (4)$$

where B_G^l is the longitudinal field of the low-field component, $\frac{dI(\lambda)}{d\lambda}$ describes the gradient of the flux profile, S is the relative area of the spot projected on the disc, λ_0 is the $H\alpha$ rest wavelength and $V(\lambda)_{spot}$ is the Stokes V profile from the strong-field component observed in the $H\alpha$ wings.

In Eq.(4) we effectively separate the disc into two equivalent areas with different averaged magnetic field strengths. The first term in the equation describes the weak-field area and the

second term is attributed to the strong-field component. The first term is used in the usual manner according to which the flux and its gradient are taken directly from the observed spectra. (Inaccuracies due to the presence of the strong-field features in the wings are comparatively weak: these features are located quite far from the line core and do not affect the narrow central low-field polarization profile). However, circular polarization $V(\lambda)_{Spot}$ from the strong-field component (the second term in the equation) cannot be fitted in the same way.

In order to fit $V(\lambda)_{Spot}$ and estimate the longitudinal field of the strong-field area, we compute:

$$V(\lambda)_{Spot} = \frac{I(\lambda)_{Spot}^L - I(\lambda)_{Spot}^R}{I(\lambda)} \quad (5)$$

where the flux $I(\lambda)$ is the observed H α flux profile, and $I(\lambda)_{Spot}^L$ and $I(\lambda)_{Spot}^R$ are the left- and right-hand polarized parts of the H α profile from the strong-field equivalent area of the disc. In the observed polarization spectra $I(\lambda)_{Spot}^L$ and $I(\lambda)_{Spot}^R$ are mixed with fluxes from the weak-field equivalent area and therefore can not be extracted directly. However, we may estimate them with some simplifications.

Individually, $I(\lambda)_{Spot}^L$ and $I(\lambda)_{Spot}^R$ are Zeeman-split profiles of the circularly polarized satellite σ components. Due to the fact that the σ_- component is absent in $I(\lambda)_{Spot}^R$, and the σ_+ component is absent in $I(\lambda)_{Spot}^L$, their centers of gravity are displaced, indicating the presence of the longitudinal field from the strong-field area. Their difference provides the non-zero circular polarization (Eqn. 5).

Because $I(\lambda)_{Spot}^L$ and $I(\lambda)_{Spot}^R$ are not resolved in the total left- and right-circularly polarized observed fluxes, the determination of their true shapes requires detailed modeling the field geometry. However, as a first-guess approximation we may describe them by simulating an equivalent “mean” Zeeman-broadened H α profile magnetically displaced to the left- and right-sides from the rest wavelength ². With this simplification only two parameters – Zeeman broadening and their magnetic displacement due to the averaged longitudinal field from the spot should be varied to reproduce the observed circular polarization.

²The low resolving power of the FORS1 and UAGS, as well as unresolved circular polarization features attributed to the strong-field area, enable us to consider the problem in terms of Zeeman broadening instead of detailed analysis of the strong-field Zeeman pattern.

In the simulation procedure we may use a template H α profile, artificially broadened to unresolved Zeeman patterns typical for $I(\lambda)_{Spot}^R$ and $I(\lambda)_{Spot}^L$ and magnetically displaced. This template can be taken from a zero magnetic field solution for the atmosphere of WD 1953-011 or from the observed spectra. For example, assuming the pressure-temperature conditions in the spot area to be similar to conditions in the other parts of the white dwarf’s surface we may choose as the template one of the observed weak-field H α profiles (obtained at those moments when the spot is not seen). In our analysis we proceed this way.

Thus, to simulate $I(\lambda)_{Spot}^L$ and $I(\lambda)_{Spot}^R$ in order to fit the circular polarization (5) from the strong-field area and estimate its longitudinal magnetic field we used the following iterative method:

- **Step-1:** We construct the reference weak-field “template” H α profile from the observed I-profiles obtained at those rotational phases where the strong-field Zeeman pattern is not seen.
- **Step-2:** We artificially broaden the template profile by a gaussian filter with an arbitrary half-width to an unresolved strong-field Zeeman pattern and displace the result by the magnetic displacement factor $\Delta\lambda$ to the shorter / longer wavelengths to estimate the $I(\lambda)_{Spot}^L$ and $I(\lambda)_{Spot}^R$ profiles.
- **Step-3:** Varying the magnetic broadening of the estimated profiles $I(\lambda)_{Spot}^L$ and $I(\lambda)_{Spot}^R$ and their Zeeman displacement we finally fit the strong-field circular polarization (5) in the working equation (4). The displacement found $\Delta\lambda = 4.67 \cdot 10^{-13} B_S^l \lambda_0^2$ (Landstreet 1980), gives an estimate of the longitudinal field B_S^l . (In other words, taking S measured from the Stokes I spectra and presented in Table 3 we simultaneously fit the observed combined Stokes V (4) varying B_G^l and circular polarization (5) of the strong-field component, where B_S^l is one of the parameters.)

In the fit procedure, the associated error bars are obtained using the Monte Carlo modeling method presented by Schmidt & Smith (1994). An example of the fit is presented in Fig. 5. The results are collected in Table 4.

This method gives quite robust estimates of the longitudinal magnetic field of the low-field component. In the case of the strong-field component, the real intensities of the fields could be slightly over or underestimated due to the simplifications described above. For these reasons, estimates of the strong-field component given here could be considered to be

approximate. As an alternative, the two-component circular polarization spectra could be analyzed by using Zeeman tomography (Euchner et al. 2002, for instance). To provide more precise modeling, below (Sec.8) we analyze our data again in the framework of simplified Zeeman tomography.

6. Period determination

To search for the star’s rotation period we used the equivalent widths EW_{core} of the $H\alpha$ core determined in Sect.4 . This observable is the most sensitive indicator for the determination of the rotation period. To determine the rotation period we applied the Lafler-Kinman method (Lafler & Kinman 1965), as modified by Goransky (2004). Analysis of the power spectrum of the data revealed a signal indicating a probable period between 1.4 and 1.5 days (Fig. 6). This is consistent with the period estimate ($P \approx 1.45$ days) given by Wade et al. (2003) and Brinkworth et al. (2005).

Detailed study of the periodogram showed that the most significant sinusoidal signal corresponds to a period $P = 1.4480 \pm 0.0001$ days. Other peaks are located around 1.447 days and 1.442 days. An examination of these periods reveals distorted, non-sinusoidal signals and we do not consider these periods further.

The phase variation of the $H\alpha$ core equivalent widths EW_{core} derived with this period is presented in Fig. 7. The derived period shows a very good agreement among all the observations taken from different telescopes (the VLT, BTA and AAT). For the minimum of EW_{core} we obtain the following ephemeris:

$$JD = 2452048.801 \pm 0.03 + 1^d.4480 \pm 0.0001 E$$

The corresponding phase curves of the mean field modulus $|B_G|$ and longitudinal field $|B_G^l|$ of the weak-field components are presented in Fig. 8. The phase curves are almost sinusoidal, and symmetric about the values of about $|B_G| = +87$ kG and $|B_G^l| = -43$ kG. The modulus of the weak-field component varies from $+77 \pm 1.5$ kG to $+97 \pm 1.5$ kG; the longitudinal magnetic field shows variation in the range -39 ± 2 kG to -47 ± 2 kG.

As one can see in Fig. 8 the behavior of the longitudinal magnetic field and modulus of the weak-field component suggest the field geometry to be a simple, low-order poloidal field, which supports our view that the period is correct. Below we use this period in analyzing the magnetic field morphology of WD 1953-011. At the same time it is important to note that another estimate of the rotational period ($P = 1.4418$ days) obtained by Brinkworth et al. (2005) from differential photometry of this MWD is similar to, but formally different from,

our result. Following the next section, where we establish the magnetic field morphology of the low-field component, we will discuss this difference in more detail.

7. Modeling the weak-field component of the magnetic field of WD 1953-011

To verify that the behavior of the weak-field component of WD 1953-011 is consistent with a nearly dipolar geometry, we have followed the schematic method proposed by Landolfi et al. (1997). This method has already been described and applied to establish the magnetic field morphology of the weak field white dwarf WD0009+501 (see Valyavin et al. (2005) for details). For this reason here we do not explain all the modeling details, but restrict ourselves to the presentation of the results.

In this paper we model the phase-resolved measurements of the mean longitudinal field and mean field modulus of the weak-field component within the framework of a pure dipole and dipole+quadrupole field. The phase-resolved observables for the weak-field component which we use as input data are obtained by binning measurements in phase and averaging. The binned data are presented in Table 5.

The dipole or dipole plus quadrupole models depend on the following 10 parameters:

- B_d and B_q , the dipole and quadrupole strength, respectively;
- v_e , the stellar equatorial velocity;
- i , the inclination of the stellar rotation axis to the line of sight;
- β , the angle between the dipolar axis and the rotation axis;
- β_1 and β_2 , the analogues of β for the directions identified by the quadrupole;
- γ_1 and γ_2 , the azimuthal angles of the unit vectors of the quadrupole;
- f_0 , the “reference” rotational phase of the model;
- $v_e \sin i$, the projected stellar rotation velocity.

The angles i , β , β_1 , β_2 range from 0° to 180° , while γ_1 , γ_2 , f_0 range from 0° to 360° . The rotational period $P = 1.448$ and the limb-darkening constant u , which also affects the expressions of the magnetic observables, are taken as fixed. (Note that the pure dipole model would retain as free parameters only B_d , v_e , i , β , and f_0 .)

For the stellar mass, Bragaglia et al. (1995) gave the value of $0.844 M_{\odot}$, which together with known surface gravity of WD 1953-011 ($\log g = 8.412$, Bragaglia et al. (1995)) correspond to a stellar radius of about $0.0095 R_{\odot}$. This parameter and the period were then used to estimate the equatorial and projected velocities of the star.

For the limb-darkening coefficient, we adopted the value of $u = 0.5$. Note that, as discussed by Bagnulo et al. (2000), the results of the modeling are only slightly influenced by the u value. The best-fit parameters are:

A) Dipole

$$\begin{aligned}
 i &= 14^{\circ} \pm 10^{\circ} \\
 \beta &= 14^{\circ} \pm 10^{\circ} \\
 f_0 &\approx 352^{\circ} \\
 B_d &= 108 \pm 5 \text{ kG} \\
 v_e &= 0.33 \pm 0.05 \text{ km s}^{-1} \\
 v_e \sin i &= 0.08 \pm 0.03 \text{ km s}^{-1}
 \end{aligned}$$

B) Dipole + quadrupole

$$\begin{aligned}
 i &= 18^{\circ} \pm 10^{\circ} \\
 \beta &= 8^{\circ} \pm 10^{\circ} \\
 f_0 &\approx 357 \\
 \beta_1 &= 22^{\circ} \pm 10^{\circ} \\
 \beta_2 &= 24^{\circ} \pm 10^{\circ} \\
 \gamma_1 &\approx 77^{\circ} \\
 \gamma_2 &\approx 243^{\circ} \\
 B_d &= 178 \pm 30 \text{ kG} \\
 B_q &= 233 \pm 30 \text{ kG} \\
 v_e &= 0.33 \pm 0.05 \text{ km s}^{-1} \\
 v_e \sin i &= 0.1 \pm 0.05 \text{ km s}^{-1}
 \end{aligned}$$

Note that, as explained by Bagnulo et al. (2000), the available observations do not allow one to distinguish between two magnetic configurations symmetrical about the plane containing the rotation axis and the dipole axis. Such configurations are characterized by

the same values of B_d , B_q , v_e , γ_1 , γ_2 , f_0 , while the remaining angles are related by

$$\begin{pmatrix} i, & \beta, & \beta_1, & \beta_2 \\ 180^\circ - i, & 180^\circ - \beta, & 180^\circ - \beta_1, & 180^\circ - \beta_2 \end{pmatrix}.$$

Due to the fact that the spin axis angle is close to a pole-on orientation and due to the small number of available observables, the error bars on the derived quantities are fairly large. For the same reasons, there are some uncertainties in the determinations of all the parameters considered together. However, despite these weakness, we are able to obtain some conclusions about the most probable geometry of the white dwarf’s global field.

The best fit of the dipole+quadrupole model applied to the observations is shown by solid lines in Fig. 9. For comparison, the dashed line shows the fit obtained using the pure dipolar morphology. As is evident, the dipolar model does not reproduce the observations well. Examination of the reduced χ_r^2 statistics shows that the quality of the dipole+quadrupole fit ($\chi_r^2 = 0.22, 0.43$ for longitudinal field and field modulus, respectively) is significantly better than the pure dipole fit ($\chi_r^2 = 1.9, 2.2$). We therefore conclude that the large-scale weak-field component of WD 1953-011 is better modeled by the superposition of a dipole and quadrupole components.

8. High-field component

8.1. Migrating magnetic flux tube?

In contrast to the well-organized, nearly sinusoidal variation of the weak-field component, the phase behavior of the high-field structure exhibits a number of peculiar features that made it impossible to model these data as a simple low-order multipole:

- According to the measurements of the Zeeman-split satellite spectral features in the $H\alpha$ wings, the mean field modulus of the strong-field component does not show any noticeable variation during the star’s rotation. (Due to rotation, we see variation of the flux intensities from the strong-field area, but the corresponding Zeeman displacement is nearly constant.) The most likely explanation (Maxted et al. 2000) is that there is an area with a nearly uniformly distributed strong magnetic field. This explanation, if true, suggests that the strong-field component has a localized geometry and cannot be understood as a high-field term in the multipolar expansion of the star’s general field. Averaging all the data we determine $\langle |B_{spot}| \rangle = 515 \pm 7$ kG.

- The Zeeman pattern attributed to the strong-field component becomes visible at rotational phases $\phi = 0.25 - 0.7$ and demonstrates variation in the flux intensities that suggests rotational variability of the projected effective size S of the magnetic spot. The projected area of the strong-field structure varies from zero to about 12% of the disk, consistent with the study of Maxted et al. (2000). This observable can be used as an additional parameter to test the rotational period of the star. However, using this quantity to search for the period we did not find a regular signal at any period within the tested 5-year time base. Moreover, phasing the data with the magnetic ephemeris characterized by the rotational period of 1.448 days, the resultant phase curve of the spot size variation (Fig. 10) appears distorted in comparison to the well-organized behavior of the weak-field component phased with the same ephemeris. We observe a small relative phase shift between the data obtained with different telescopes that may indicate a possible secular longitudinal drift of the strong-field component.
- The averaged longitudinal field of the strong field area varies from zero (when the area is invisible) to about 450 kG (Table 4) which is comparable to the averaged mean field modulus (≈ 515 kG) of the field. This suggests a deviation of the strong field component from any of low-order multipolar geometries for which the difference between the full vector and its longitudinal projection should be much larger (for example, for a centered dipole field the difference should be at least 2.5 times, Stibbs (1950)).

The last point suggests the presence of an essentially vertical orientation of the magnetic field lines relative to the star’s surface, typical for local magnetic flux tubes in cool, convective stars (the Sun for example). If the geometry is a tube seen as a local magnetic spot in the photosphere, we may also expect the above-mentioned secular drift. To our knowledge and by an analogy to the Sun, such fields are expected to show dynamical activity like migration over the star’s surface and be associated with dark spots that might produce photometric variability of the star. Significant photometric variability of WD 1953-011 has been established (Wade et al. 2003; Brinkworth et al. 2005). However, in this paper we are unable to establish the association of the darkness and magnetic spots for reasons which we discuss below.

8.2. Geometry and location of the magnetic spot

Measuring the longitudinal magnetic field of the strong-field component as described in Sect. 5 we noted that the estimates of the longitudinal field of the strong-field area might be affected by our simplifying assumptions. In order to control these measurements we have

also directly modeled the observed polarization and intensity $H\alpha$ spectra of the star without parametrizing the surface field components. In addition to the analysis of the Stokes I and V spectra, the observed Q and U spectra were also taken into consideration. As can be seen in Fig. 1, linear polarization Stokes Q, U signatures are detected only marginally at a few rotational phases. However, this information can also be used to constrain the magnetic geometry of the degenerate. Note that different magnetic geometries may produce similar Stokes V spectral features due to axial symmetry of circular polarization provided by the longitudinal projection of the field. Linear polarization restricts the strength and orientation of the transverse field that, together with circular polarization, makes it possible to resolve the geometry spatially. The observed Q and U spectra are mainly noise, but we may try to use them in terms of the upper limits.

In our model we examined several low order multipolar magnetic field geometries, integrating over the surface elementary (taken at a single surface element) Stokes I, V, Q , and U spectra calculated for various field strengths and orientations of the magnetic field lines. The technique we used to calculate the elementary spectra deserves some special explanation.

a) Simulation of the Stokes I, V, Q and U synthetic $H\alpha$ spectra.

Generally, accurate simulation of the split Balmer profiles in spectra of strong magnetic white dwarfs requires detailed computations of the main opacity sources under the influence of strong magnetic fields. To our knowledge, these computations have not yet been tabulated for practical use. For this reason, a self-consistent solution of the transfer equation for the line profiles in spectra of strong-magnetic white dwarfs cannot be performed without special consideration of additional parameters (related, for example, to the Stark broadening in the presence of a strong magnetic field, Jordan (1992)). However, in case of the weak-field degenerates we may restrict ourself to a zero-field solution similar to that presented by Wickramasinghe & Martin (1979) or by Schmidt et al. (1992). The method assumes that if the Stark broadening dominates the line opacity, the total opacity can be calculated as the sum of individual Stark-broadened Zeeman components. The Stark broadening is suggested to be taken as “non-magnetic” in this case. Under these simplifying assumptions we may simulate the local, elementary Zeeman spectra using one of the following two ways:

- i to compute the transfer equation for all Stokes parameters at given strength and orientation of a local magnetic field line calculating the $H\alpha$ opacities as described, or (alternatively)
- ii to select a “template” $H\alpha$ profile typical for a zero-field white dwarf with the same

pressure-temperature conditions as in WD 1953-011 for construction of the elementary Zeeman spectra. (In other words, we may try to construct from this template profile individual Zeeman π - and σ - components, parametrizing their magnetic displacement and relative intensities, and additively combine them to obtain the elementary I, V, Q, U $H\alpha$ profiles.)

The first, direct method of atmospheric calculations for WD 1953-011 requires special theoretical tools which are outside the scope of this observational paper. The second, simplified method, which we will use, seems to be rather rough due to the fact that the fluxes from the individual π - and σ - components obtained by using the zero-field template profile are generally not additive (whereas their corresponding opacities can be added in the transfer equation). Nevertheless, in the linear guess approximation they can be taken as additive and the method can also be applied. Besides, testing this method on some standard, well-studied magnetic Ap/Bp stars we have obtained satisfactory results modeling their observed polarizations. This allowed us to conclude that the method is reasonably accurate.

Thus, to calculate the elementary I, V, Q, U $H\alpha$ profiles we adopted the use of the zero-field $H\alpha$ template profile which was constructed from the observed I-spectra obtained at those moments, when the strong-field Zeeman pattern is not seen. The Stark parts of the profile were obtained by averaging the I profiles at the rotation phases 0 and 0.91 (see Fig. 1) in which the strong-field features are not seen. The central “zero-field” Doppler profile was adopted to reproduce in the model procedure the observed low-field magnetic broadening of the $H\alpha$ cores at phases 0 and 0.91. The necessary individual profiles of the non-displaced π - and displaced σ - components were obtained by entering the normal Zeeman displacements according to the orientation of the local magnetic field: the circularly polarized σ - components are displaced according to the longitudinal projection of the local magnetic field, and the linearly polarized σ - components are displaced by the transverse field.

In order to model the polarization $H\alpha$ profiles, the relative intensities of the central π - and displaced $\sigma\pm$ components were computed from the projection of the local field vector onto the plane on the sky and on the line of sight as described by Unno (1956) (for a qualitative explanation see also Landstreet (1980)). The final intensities of the π - and σ - components were obtained by renormalisation such that the total sum of the fluxes from all the components be equal to the flux from the zero-field template $H\alpha$ profile.

Finally, the elementary π - and σ - components were combined to construct from them the elementary I, V, Q, U spectra by simulation of the ordinary and extraordinary beams given by a polarimetric analyzer. For example, simulating the $H\alpha$ Stokes V profile, all the components except the circularly polarized σ - components are equally distributed between

the beams. The circularly polarized σ_+ components are absent in one of the beams, and the oppositely polarized σ_- components are absent in the other beam. The final Stokes V $H\alpha$ profile was obtained by subtraction of the ordinary from extraordinary beams and division of the result by the total flux. The Q and U spectra were obtained in a similar way: the linearly polarized σ components and central π component are distributed between the beams according to the projection of the local magnetic field onto the plane of the sky.

After the determination of the elementary I, V, Q, U spectra given by a magnetic geometry in all surface elements, we finally integrated and averaged them over the disc. For the limb-darkening coefficient we adopted the value of $u = 0.5$.

b) Modeling the field geometry in WD 1953-011 by simulation of the observed polarization spectra.

In Sect. 5) we have concluded, that estimates of the longitudinal magnetic field based on the weak-field approximation are accurate enough to make it possible to model the geometry of the low-field component separately from the strong-field component in the manner as demonstrated in Sect. 7. For this reason, and in order to reduce a number of variables, we use those results (obtained in Sect. 7) as input and non-changeable parameters in the tomography. We just note, that modeling the observed spectra obtained at those time moments, where the spot is not seen, we have confirmed, that the observations (Stokes- V spectra) can be better fit by the dipole+quadrupole geometry of the low-field component with parameters performed in Sect. 7 (case B). Examination of the pure dipole model (case A) gives no satisfactory results and we do not use this case here.

Modeling the strong-field area as an additional harmonic in the low-order (lower than octupole) multipolar expansion we were unable to reproduce the observations. The fit does not provide the necessary contrast in the observed Zeeman patterns at those phases where the polarization and intensity spectra demonstrate the weak- and strong-field Zeeman features together. However, assuming the strong-field component to be concentrated into a localized area having maximum projected size of about 12 per cent of the disk, the strong-field Zeeman spectral features can be well-reproduced with an average magnetic field of 550 ± 50 kG. Practically the same result has been obtained by Maxted et al. (2000).

To model the strong-field area we tested two simplified localized geometries: a “contrast spot” with a homogeneously distributed, essentially vertical magnetic field, and a “sagittal” geometry with a strong vertically-oriented central magnetic field, that smoothly decreased to zero at the spot edges. Generally, both geometries are able to describe the Stokes I and V spectra with more or less acceptable accuracy. The first model, however, does not provide us

with a good fit of the Q and U spectra due to the presence of the sharp (and non-physical) jump of the field intensity at the edges of the strong-field area. For this reason we do not discuss this case in detail.

The “sagittal” geometry of the strong-field area was constructed by using a modified model of a centered dipole: about 45% of the spot’s area (central parts) have the dipolar distribution with polar field $Bp = +810$ kG at the center. The remaining 55% of the external dipolar field is artificially modulated to have a gradual decrease to zero at the edges of the area. This model provides a good fit of the Stokes I, V spectra and reasonable reproduction of the linear polarization Q, U -spectra, as shown in Fig.11 where we also illustrate the tomographic portrait of the white dwarf’s magnetosphere.

Despite the fact that we obtain such a good agreement of the “sagittal” geometry with the observables from the strong-field area, we do not claim that this geometry is fully correct in all details (for example, the model does not control conservation of magnetic flux). Similar to the case of the weak-field component, the most natural way to study the strong-field area is to describe it as a strong-field feature resulting from the superposition of several high-order harmonics in the multipolar expansion. At this time we are unable to study this term using any combination of the first harmonics higher than octupole, but we do not exclude that the use of the highest terms of different polarities and intensities will resolve the problem.

However, this result clearly demonstrates a qualitative difference in the morphologies of the strong-field area and the global field of the white dwarf. From the model we establish with a very high probability that the strong-field area has a localized structure with essentially vertical orientation of the magnetic field lines. The physical size of the area is about 20% of the star’s surface giving maximum 12% projection on the disc. The spot is located at an angle of about 67° with respect to the spin axis, providing a maximum longitudinal field strength of about 400 kG. These results are in good agreement with the measurements of the longitudinal field of the spot.

9. Discussion

We have presented new low-resolution spectropolarimetric observations of the magnetic white dwarf WD 1953-011. From these observations and observations of previous authors we have determined the star’s rotation period, mean longitudinal field, mean field modulus, and surface field morphology. Let us finally summarize these results.

- 1) Our present picture of WD 1953-011 consists of a MWD with relatively smooth, low-field global magnetic field component, and a high-field magnetic area.

- 2) The low-field component demonstrates regular periodicity with period $P = 1.4480 \pm 0.0001$ days. We interpret this as the rotational period of the white dwarf. The long-term stability of the surface and longitudinal magnetic fields of the low-field component enable us to interpret this component as a fossil poloidal magnetic field consisting of dipolar and quadrupolar harmonics with the following basic parameters:
- 1) the inclination of stellar rotation axis $i = 18^\circ \pm 10^\circ$;
 - 2) the angle between the dipolar axis and the rotation axis $\beta = 8^\circ \pm 10^\circ$;
 - 3) the dipole strength $B_d = 178 \pm 30$ kG;
 - 4) the quadrupole strength $B_q = 233 \pm 30$ kG.
- 3) The strong-field component exhibits a peculiar localized structure. The mean field modulus of the spot $|B_{spot}|$ is estimated to be 515 ± 7 kG, which is consistent with the results presented by Maxted et al. (2000). The longitudinal magnetic field of the spot varies with rotational phase from < 300 kG to about 400 kG. Comparing the mean field modulus with the maximum longitudinal field we suggest that the geometry of the high-field spot may be similar to a magnetic flux tube with vertically-oriented magnetic field lines. The spot is located at an angle of $\approx 67^\circ$ with respect to the spin axis.

Our results suggest that the magnetic field of WD 1953-011 consists of two physically different morphologies - the fossil poloidal field and an apparently induced magnetic spot. To our knowledge, fossil, slowly decaying global magnetic fields are organized in a nearly force-free poloidal configuration³. In contrast, if the suggested vertical orientation of the magnetic field lines in the spot is correct, the uncompensated “magnetic pressure”³ of such a localized field may dominate against the tension causing a strong impact on the pressure-temperature balance in the photosphere of the degenerate. This may produce a temperature difference between the strong-field area and other parts of the star’s surface. As a result we may expect rotationally-modulated photometric variability of WD 1953-011 (as observed by Wade et al. (2003) and Brinkworth et al. (2005)). For these reasons (and by analogy to sunspots) such fields might be unstable if not supported by other dynamical processes such as differential rotation, and may therefore exhibit secular drift with respect to the stellar rotation axis.

³According to the basic properties of the Maxwell stress tensor (see, for instance, Parker (1979)) the magnetic field \mathbf{B} creates in the atmospheric plasma an isotropic pressure $\frac{B^2}{8\pi}$ and tension $\frac{B_i B_j}{4\pi}$ directed along the magnetic lines of force. While neighboring lines of force of a magnetic field try to expand due to the magnetic pressure, tension tends to compensate for this effect. The force-free configuration is possible only when the gradient of the magnetic pressure is fully compensated by the tension forces.

In the above context we note that significant photometric variability of WD 1953-011 has been established (Wade et al. 2003; Brinkworth et al. 2005). Also, remarkably, the authors had encountered problems analyzing the periodicity of the variable differential flux. When individual epochs of their photometric data are phased according to the rotation period of about 1.45 days, the resultant folded lightcurves are smooth and approximately sinusoidal. However, they had difficulty obtaining an acceptable fit to all epochs of photometric data considered simultaneously (Wade et al. 2003). Besides, periodograms (Brinkworth et al. 2005) obtained separately for their 7 individual observing runs indicate *a significant spread in the period distribution*. The individual peaks are stochastically distributed around a rotation period $P \approx 1^d.45$ from $P \approx 1^d.415$ to $P \approx 1^d.48$, also suggesting a probable phase shift from epoch to epoch with characteristic times from tens to hundred of days. Combining all the data, they establish their version of the rotation period $P = 1.^d441769(8)$ days. This period is significantly different from the period derived by us from the behavior of the global field of the star ($P = 1.448 \pm 0.0001$ days).

Indirectly, these facts suggest a physical relationship between the darkness and magnetic spots, and their possible secular migration. Unfortunately, our spectroscopy and the available photometry were obtained at different epochs, making it impossible to study this relationship in this paper. Examination of these problems will be among the goals of our further study of this magnetic degenerate upon carrying out the necessary simultaneous photometric and spectral observations of this star.

Our thanks to L. Ferrario, P. Maxted, and C. Brinkworth for providing details of individual spectroscopic and photometric measurements of WD 1953-011. We are also especially grateful to Stefan Jordan (our referee) for valuable comments, suggestions and his high estimation of our work. GV is grateful to the Korean MOST (Ministry of Science and Technology, grant M1-022-00-0005) and KOFST (Korean Federation of Science and Technology Societies) for providing him an opportunity to work at KAO through the Brain Pool program. GAW and JDL acknowledge Discovery Grant support from the Natural Sciences and Engineering Research Council of Canada. This study was also partially supported by KFICST (grant 07-179). Based on observations collected at the European Southern Observatory, Chile (ESO program 67.D-0306(A))

REFERENCES

- Angel, J.R.P., McGraw, J.T. & Stockman, H.S., 1973, ApJ, 184, L79
Angel, J.R.P., Borra, E.F., & Landstreet, J.D., 1981, ApJS, 45, 457

- Appenzeller, I., 1967, *PASP*, 79, 136
- Appenzeller, I., Fricke, K., Furtig, W., et al., 1998, *The Messenger*, 94, 1.
- Afanasiev, V.L., Burenkov, A.N., Vlasyuk, V.V. & Drabek S.V., 1995, SAO Ras internal rep., 234
- Aznar Cuadrado, R., Jordan, S., Napiwotzki, R., Schmid, H.M., Solanki, S.K., & Mathys, G., 2004, *A&A*, 423, 1081
- Bagnulo, S., Landolfi, M., Mathys, G., & Landi Degl’Innocenti, M., 2000, *A&A*, 358, 929
- Bagnulo, S., Szeifert, T., Wade, G., Landstreet, J., Mathys, G., 2002, *A&A*, 389, 191
- Barstow, M.A., Jordan, S., O’Donohue, D., Burleigh, M.R., Napitowski, R., & Harrop-Alin, M.K., 1995, *MNRAS*, 277, 971
- Bragaglia, A., Renzini, A., & Bergeron, P., 1995, *ApJ*, 443, 735
- Brinkworth, C.S., Marsh, T.R., Morales-Rueda, L., Maxted, P.F.L., Burleigh, M.R., & Good, S.A., 2005, *MNRAS*, 356, 89
- Euchner, F., Jordan, S., Beuermann, K., Gänsicke, B.T., and Hessman, F.V., 2002, *A&A* 390, 633
- Fabrika, S.N., Valyavin, G.G., & Burlakova, T.E., 2003, *Astronomy Letters*, 29, 737
- Goransky, V., 2004, private communication.
- Jordan, S., 1992, *A&A*, 265, 570
- Jordan, S., Aznar Cuadrado, R., Napiwotzki, R., Schmidt, H.M., & Solanki, S.K., 2007, *A&A*, 462, 1097
- Kawka, A., Vennes, S., Schmidt, G.D., Wickramasinghe, D.T., & Koch, R., 2007, *ApJ*, 654, 499
- Koester, D., Dreizler, S., Weidemann, V., & Allard, N.F. 1998, *A&A*, 338, 612
- Landolfi, M., Bagnulo, S., Landi Degl’Innocenti, E., Landi Degl’Innocenti, M., & Leroy, J.L., 1997, *A&A* 322, 197
- Landstreet, J.D. 1980, *Astronomical Journal*, 85, 611
- Liebert, J., Bergeron, P., & Holberg, J.B. 2003, *AJ*, 125, 348

- Lafler, J., & Kinman, T.D., 1965, ApJS, 11, 216
- Maxted, P.F.L., Ferrario, L., Marsh, T.L., Wickramasinghe, D.T., 2000, MNRAS, 315, L41
- Naydenov, I.D., Valyavin, G.G., Fabrika, S.N., et al 2002, Bull. Spec. Astrophys. Obs., 53, 124
- Parker, E. N. 1979, *Cosmical magnetic fields*, Oxford: Clarendon press
- Putney, A. 1999, 11th. European Workhop on White Dwarfs, ASP Conf. Series, 196, 195. J.E., Solheim, E.G., Meistas ed.
- Schmidt, G.D. & Northworthy, J.N., 1991, ApJ, 366, 270
- Schmidt, G.D., Bergeron, P., Liebert, J., & Saffer, Rex A., 1992, ApJ, 394, 603
- Schmidt, G.D. & Smith, P.S., 1994, ApJ, 423, L63
- Schmidt, G.D. & Smith, P.S., 1995, ApJ, 448, 305
- Stibbs, D.W.N., 1950, MNRAS, 110, 395
- Unno, W., 1956, PASJ, 8, 108
- Valyavin, G.G., Burlakova, T.E., Fabrika, S.N, & Monin, D.N., 2003, Astronomy Reports, 47, 589
- Valyavin, G.G., Bagnulo, S., Monin, D.N., Fabrika, S.N, Lee, B.-C., Galazutdinov, G., Wade, G.A., & Burlakova, T. 2005, A& A, 439, 1099
- Valyavin, G.G., Bagnulo, S., Fabrika, S.N, Reisenegger, A., Wade, G.A., Han, Inwoo, & Monin, D.N., 2006, ApJ, 648, 559
- Wade, G.A., Bagnulo, S., Szeifert, T., Brinkworth, C., Marsh, T., Landstreet, J.D., Maxted, P. 2003, in: Solar Polarization, J. Trujillo Bueno & J. Sánchez Almeida (eds.), ASP Conference Series No. 307, p. 565
- Wickramasinghe, D.T., & Martin, B. 1979, MNRAS, 188, 165

Table 1: Spectral and spectropolarimetric observations of WD 1953-011: column 1 is the Julian Date of the midpoint of the observation, column 2 is the exposure time, and column 3 reports the telescope used in the observations (**AAT** indicates the high resolution spectroscopy presented by Maxted et al. (2000)). For data obtained with the VLT the exposure times are presented for the three consecutive $I, V / Q / U$ modes of observations (in this case the midpoint corresponds to observations of the Stokes I, V parameters).

JD	<i>Exp</i> (sec)	Stokes	Telescope
2450676.955	600	I	AAT
2451391.948	600	I	AAT
2451391.955	600	I	AAT
2451391.962	600	I	AAT
2451392.059	1800	I	AAT
2451392.957	1800	I	AAT
2451393.066	1800	I	AAT
2451393.106	1800	I	AAT
2451393.943	1200	I	AAT
2451393.958	1200	I	AAT
2451393.973	1200	I	AAT
2451393.988	1200	I	AAT
2451394.003	1200	I	AAT
2452048.801	840/1200/1200	$I, V/Q/U$	VLT
2452048.893	840/1200/1200	$I, V/Q/U$	VLT
2452076.671	840/1200/1200	$I, V/Q/U$	VLT
2452076.883	840/1200/1200	$I, V/Q/U$	VLT
2452078.722	840/1200/1200	$I, V/Q/U$	VLT
2452078.879	840/1200/1200	$I, V/Q/U$	VLT
2452079.672	840/1200/1200	$I, V/Q/U$	VLT
2452079.892	840/1200/1200	$I, V/Q/U$	VLT
2452087.621	840/1200/1200	$I, V/Q/U$	VLT
2452087.670	840/1200/1200	$I, V/Q/U$	VLT
2452087.722	840/1200/1200	$I, V/Q/U$	VLT
2452087.768	840/1200/1200	$I, V/Q/U$	VLT
2452505.290	3600	I, V	BTA
2452505.327	3600	I, V	BTA
2452505.360	3600	I, V	BTA
2452505.397	3600	I, V	BTA

Table 2: Determinations of the mean modulus $|B_G|$ of the weak-field component. Column 1 is the Julian Date, Col. 2 and Col. 3 are the equivalent widths of the H α core (EW_{core}) and associated error bar, Col. 4 and Col. 5 are the inferred field strength $|B_G|$ and its error bar σ (kG), Col. 6 is the telescope used. Uncertainties at the measured equivalent widths are calculated as a noise fraction of the flux (due to Poisson noise) in the total flux under the line profile. The mean field modulus and its uncertainty obtained from the high-resolution spectroscopy with the **AAT** are taken from Maxted et al. (2000). Uncertainties at the calibrated field strengths (observations with the **VLT** and **BTA**) result from regression errors in the $EW_{core} - |B_G|$ relationship shown in Fig. 4.

JD	EW_{core}	σ	$ B_G $ (kG)	σ (kG)	Telescope
2450676.955	1.040	0.008	91	5	AAT
2451391.948	1.073	0.008	93	4	AAT
2451391.955	1.105	0.016	100	4	AAT
2451391.962	1.045	0.008	93	4	AAT
2451392.059	1.068	0.012	93	2	AAT
2451392.957	0.905	0.012	83	1	AAT
2451393.066	0.943	0.012	80	2	AAT
2451393.106	0.933	0.012	83	1	AAT
2451393.947	1.008	0.020	92	3	AAT
2451393.958	1.013	0.016	87	2	AAT
2451393.973	0.945	0.016	84	2	AAT
2451393.988	0.935	0.020	84	2	AAT
2451394.003	0.981	0.020	83	2	AAT
2452048.801	0.901	0.012	80	3	VLT
2452048.893	0.917	0.012	81	3	VLT
2452076.671	1.012	0.012	89	3	VLT
2452076.883	1.057	0.016	93	3	VLT
2452078.722	1.013	0.016	89	3	VLT
2452078.879	0.939	0.012	83	3	VLT
2452079.672	1.052	0.016	93	3	VLT
2452079.892	1.102	0.012	97	3	VLT
2452087.621	0.952	0.016	82	3	VLT
2452087.670	0.939	0.016	83	3	VLT
2452087.722	0.911	0.016	78	3	VLT
2452087.768	0.921	0.016	79	3	VLT
2452505.290	0.978	0.020	84	4	BTA
2452505.327	1.000	0.020	88	4	BTA
2452505.360	1.028	0.020	91	4	BTA
2452505.397	1.034	0.020	91	4	BTA

Table 3: Determinations of the mean modulus $|B_{spot}|$ of the strong-field component. Column 1 is the Julian Date, Col. 2 and Col. 3 are relative area of the spot on the disc S (in percent of the full disc area) and associated error bar obtained as a noise fraction of the flux in the total flux under the strong-field satellite features. Col. 4 and Col. 5 are the magnetic field strength $|B_{spot}|$ and its error bar σ (kG) obtained as uncertainty in the determination of the satellite positions deblended by Gaussians. Col. 6 is the telescope used.)

JD	$S(\%)$	σ (%)	$ B_{spot} $ (kG)	σ (kG)	Telescope
2450676.955	13.1	0.6	521	40	AAT
2451391.948	9.5	0.6	513	30	AAT
2451391.955	12.0	1.2	495	30	AAT
2451391.962	11.7	0.6	494	30	AAT
2451392.059	12.0	0.6	527	15	AAT
2451392.957	0.9	0.9	invisible		AAT
2451393.066	0.6	0.9	invisible		AAT
2451393.106	0.7	0.9	invisible		AAT
2451393.947	5.4	1.5	invisible		AAT
2451393.958	2.4	1.2	invisible		AAT
2451393.973	0.6	1.2	invisible		AAT
2451393.988	0.7	1.5	invisible		AAT
2451394.003	0.7	1.5	invisible		AAT
2452048.801	0.6	0.9	invisible		VLT
2452048.893	0.6	0.9	invisible		VLT
2452076.883	7.8	1.2	520	15	VLT
2452078.622	3.2	1.2	invisible		VLT
2452078.879	0.5	1.2	invisible		VLT
2452079.672	8.4	1.2	529	30	VLT
2452079.892	12.3	0.9	511	15	VLT
2452087.621	0.6	1.2	invisible		VLT
2452087.670	0.6	1.2	invisible		VLT
2452087.722	0.7	1.2	invisible		VLT
2452087.768	0.6	1.2	invisible		VLT
2452505.290	10.4	1.2	500	35	BTA
2452505.327	12.3	1.2	492	40	BTA
2452505.360	12.3	1.2	524	35	BTA
2452505.397	10.8	1.5	502	45	BTA

Table 4: Determinations of the longitudinal magnetic field of the low- and high-field components of WD 1953-011. Column 1 is the Julian Date, Col. 2 and Col. 3 are the longitudinal field of the low-field component and associated error bar, Col. 4 and Col. 5 are the deduced longitudinal magnetic field of the strong-field component and its error bar (“no” means “below the detection level”), Col. 6 is the telescope used.)

JD	B_G^l (kG)	σ (kG)	B_l^s (kG)	σ (kG)	OBS
2452048.801	-41.5	1.5	no		VLT
2452048.893	-39.6	1.6	no		VLT
2452076.883	-41.0	1.6	430	70	VLT
2452078.722	-42.9	1.8			VLT
2452078.879	-42.2	1.7	no		VLT
2452079.672	-41.9	1.6	360	60	VLT
2452079.892	-46.8	1.7	460	60	VLT
2452087.621	-41.5	1.6	no		VLT
2452087.670	-39.8	1.7	no		VLT
2452087.722	-40.1	1.7	no		VLT
2452087.768	-40.1	1.5	no		VLT
2452505.290	-46.2	2.3	440	80	BTA
2452505.327	-44.8	2.3	450	80	BTA
2452505.360	-45.0	2.5	no		BTA
2452505.397	-42.0	2.7	no		BTA

Table 5: Phase-resolved observable magnetic quantities of the weak-field component of WD 1953-011. The first column is rotation phase ϕ obtained according to the magnetic ephemeris characterized by the rotational period of 1.448 days found here; the second and third columns are the mean field modulus or “surface magnetic field” $|B_G|$ and associated error bar; the fourth and fifth columns are the longitudinal field B_G^l and its error bar.

ϕ	$ B_G $ (kG)	σ (kG)	B_G^l (kG)	σ (kG)
0.05	81.5	4	-40.5	1.3
0.15	82	2		
0.25	89	3		
0.35	94	3	-44	1.5
0.45	93	2		
0.55	97	3	-47	2
0.65	89	3		
0.75	86	4	-42.2	2
0.85	83	1	-41	1
0.95	78	2	-40	1

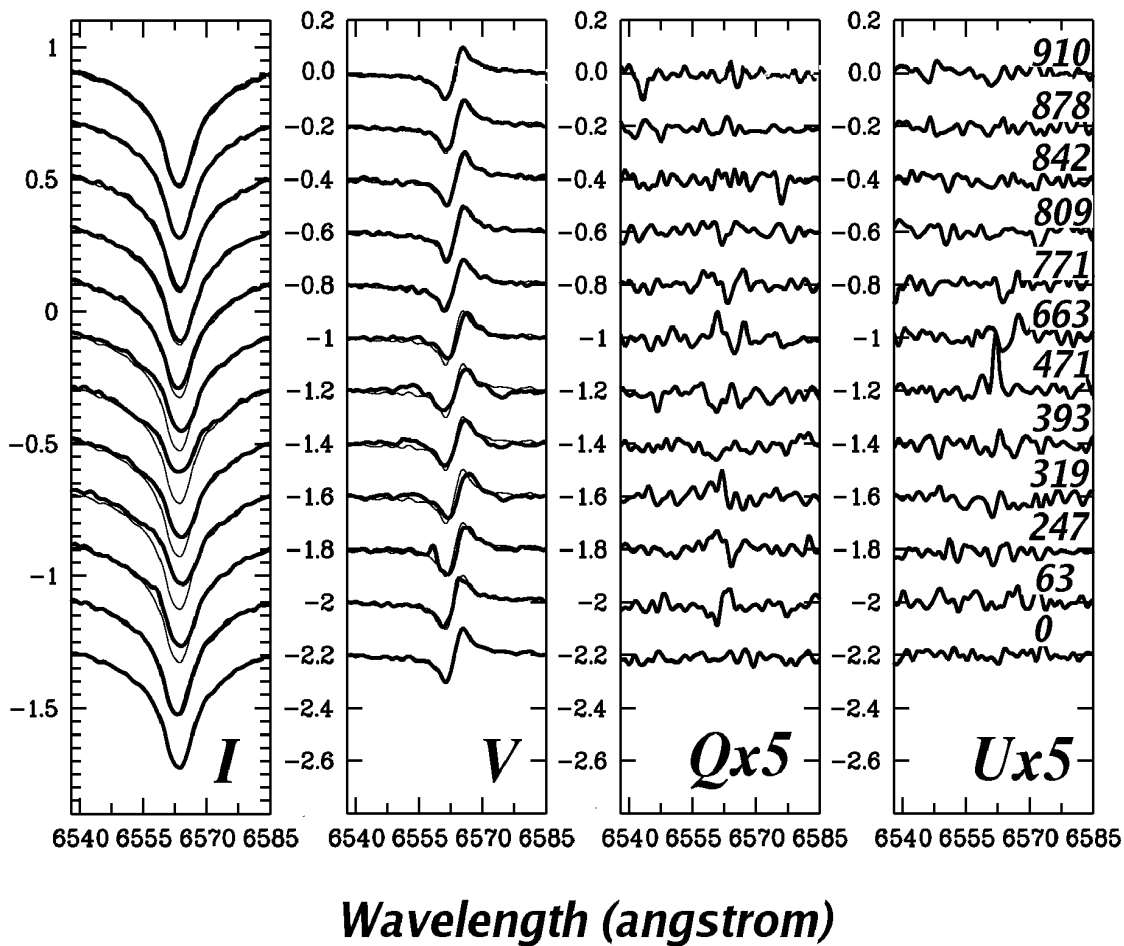


Fig. 1.— Stokes *IQUV* H α profile timeseries of WD1953-011, obtained using the FORS1 spectropolarimeter at the ESO VLT. Phases correspond to the magnetic ephemeris obtained in this paper and are expressed in part per mil at right. The thin lines represent the observations obtained at phase 0, and are reproduced to emphasise the variability of the Stokes profiles.

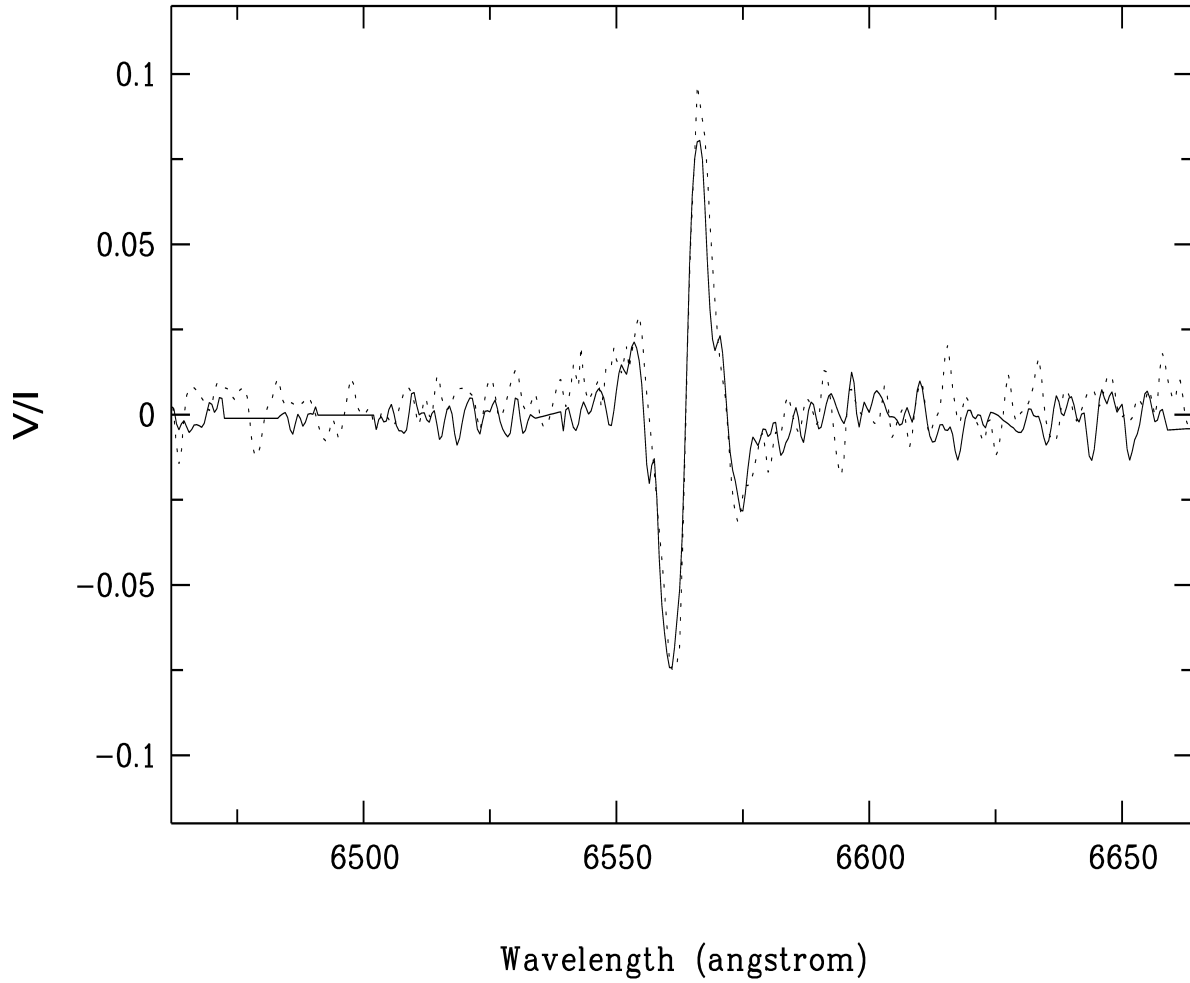


Fig. 2.— Stokes V at the $H\alpha$ line obtained with the VLT (the solid line) and the BTA (the dashed line). The spectra correspond to phases of the maximum visible strong-field Zeeman satellite features at the $H\alpha$ wings ($\phi \approx 0.3$ in observations with the BTA and $\phi \approx 0.5$ in observations with the VLT: the observed phase shift is discussed in Sect. 8 and Sect. 9 of this study.)

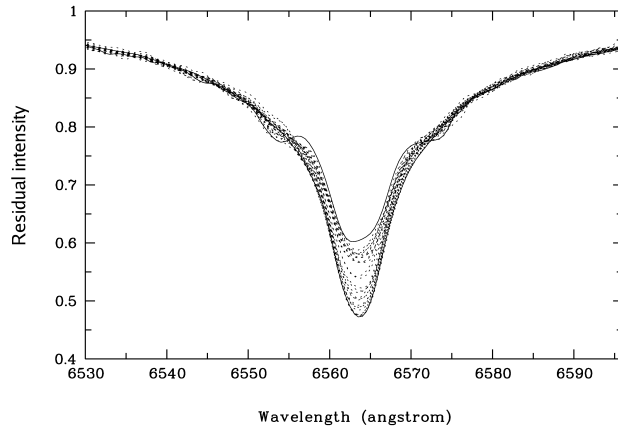


Fig. 3.— The $H\alpha$ profiles obtained at the VLT, AAT and BTA. High resolution spectra are convolved to the spectral resolution of the FORSE1 and UAGS. The solid lines illustrate profiles at two extreme rotation phases at which the spot component is most clearly seen (the shallowest profile) and where the spot component is absent (the deepest profile).

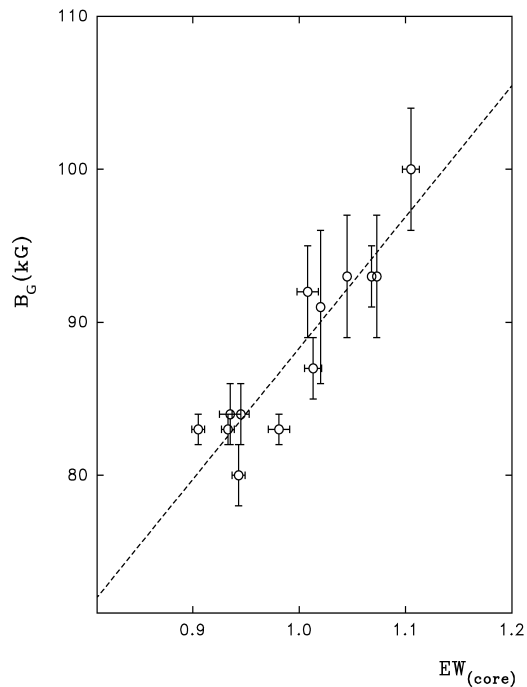


Fig. 4.— The relationship $EW_{core} - |B_G|$ obtained from the convolved high-resolution spectra for which $|B_G|$ values are estimated by Maxted et al. (2000). The dotted line is a linear fit of the relationship.

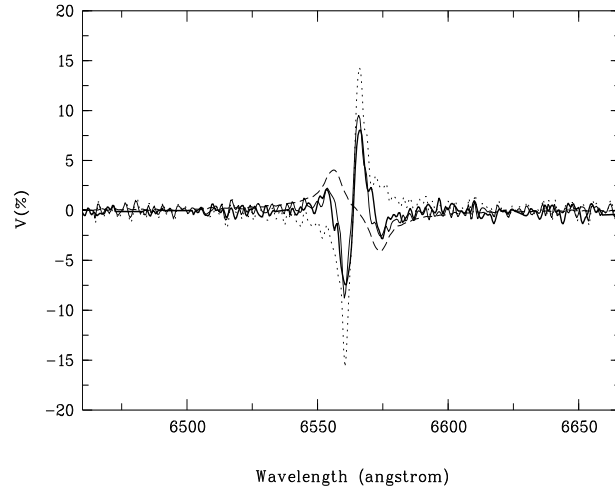


Fig. 5.— An example of the model technique as described in sect. 5. The thick solid line is the Stokes V observed spectrum containing strong circular polarization from the strong-field component; the dotted and dashed lines are modeled Stokes V spectra of the weak- and strong-field components respectively; the thin solid line is their sum.

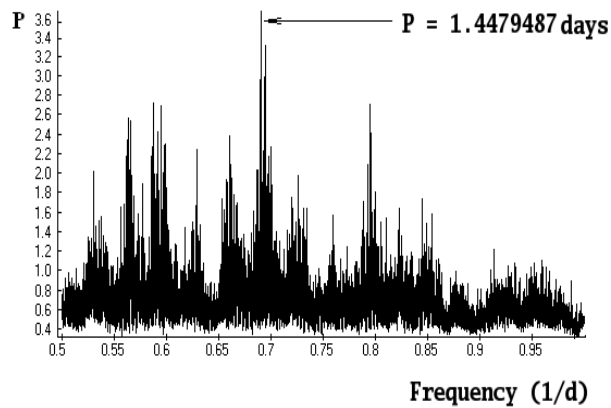


Fig. 6.— Power spectrum of the magnetic field variations in WD 1953-011.

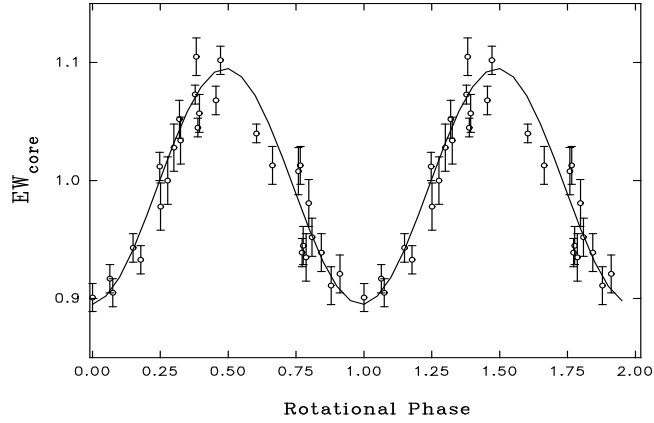


Fig. 7.— The phase curve of the equivalent widths at the H α core phased with the 1.4480-day period.

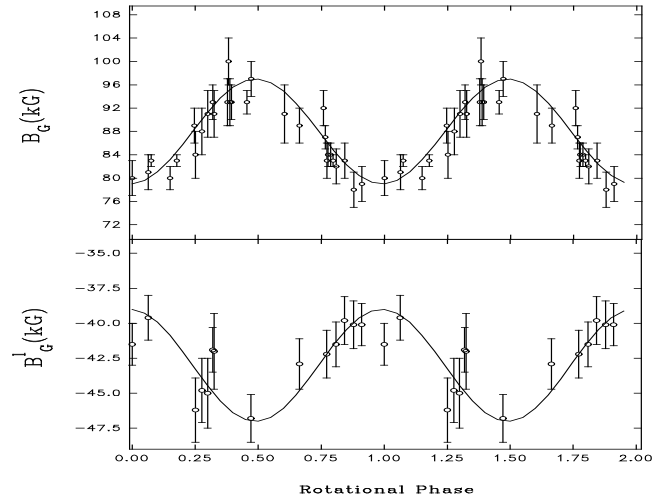


Fig. 8.— The magnetic phase curves of WD 1953-011 and their fits with the 1.448-day period. The upper plot illustrates variation of the field modulus of the weak-field component; the lower plot is variation of the its longitudinal magnetic field.

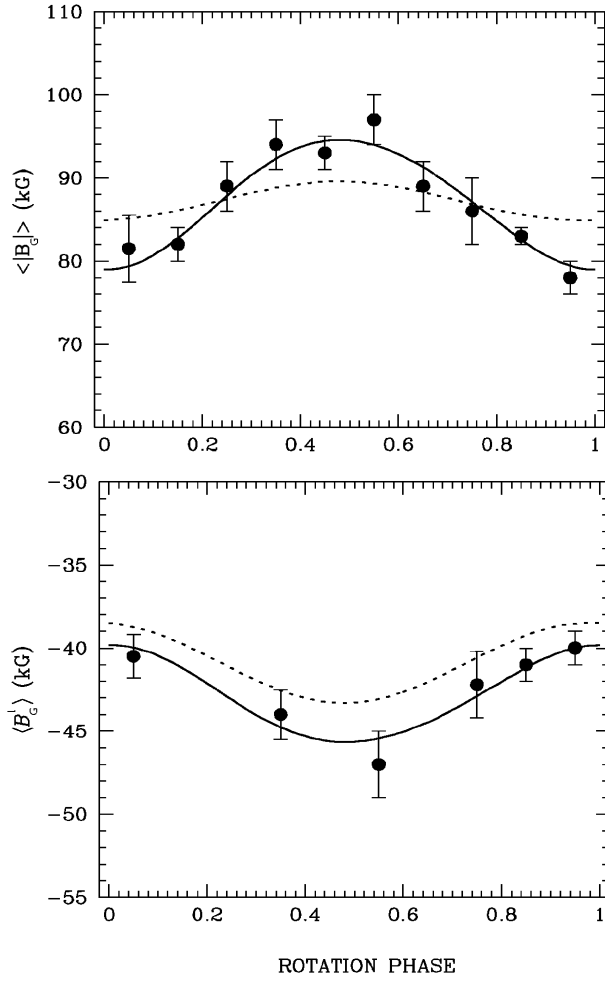


Fig. 9.— Observations and modeling of mean longitudinal field (bottom panel) and mean field modulus, or surface field (top panel). The dashed lines show a fit obtained with dipole model. The solid lines show the best-fit obtained by means of a dipole + quadrupole model.

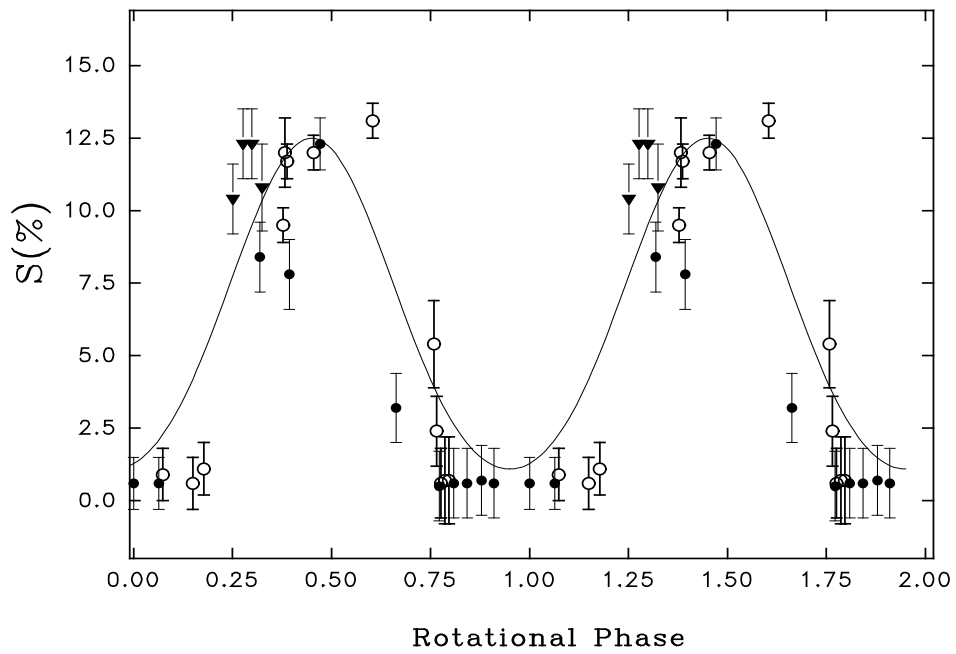


Fig. 10.— Phase-resolved projection S of the strong-field area: open circles illustrate the data from the AAT, filled circles and triangles are the observations with the VLT and BTA respectively. All the data have been phased according to the magnetic ephemeris obtained in Sect. 6.

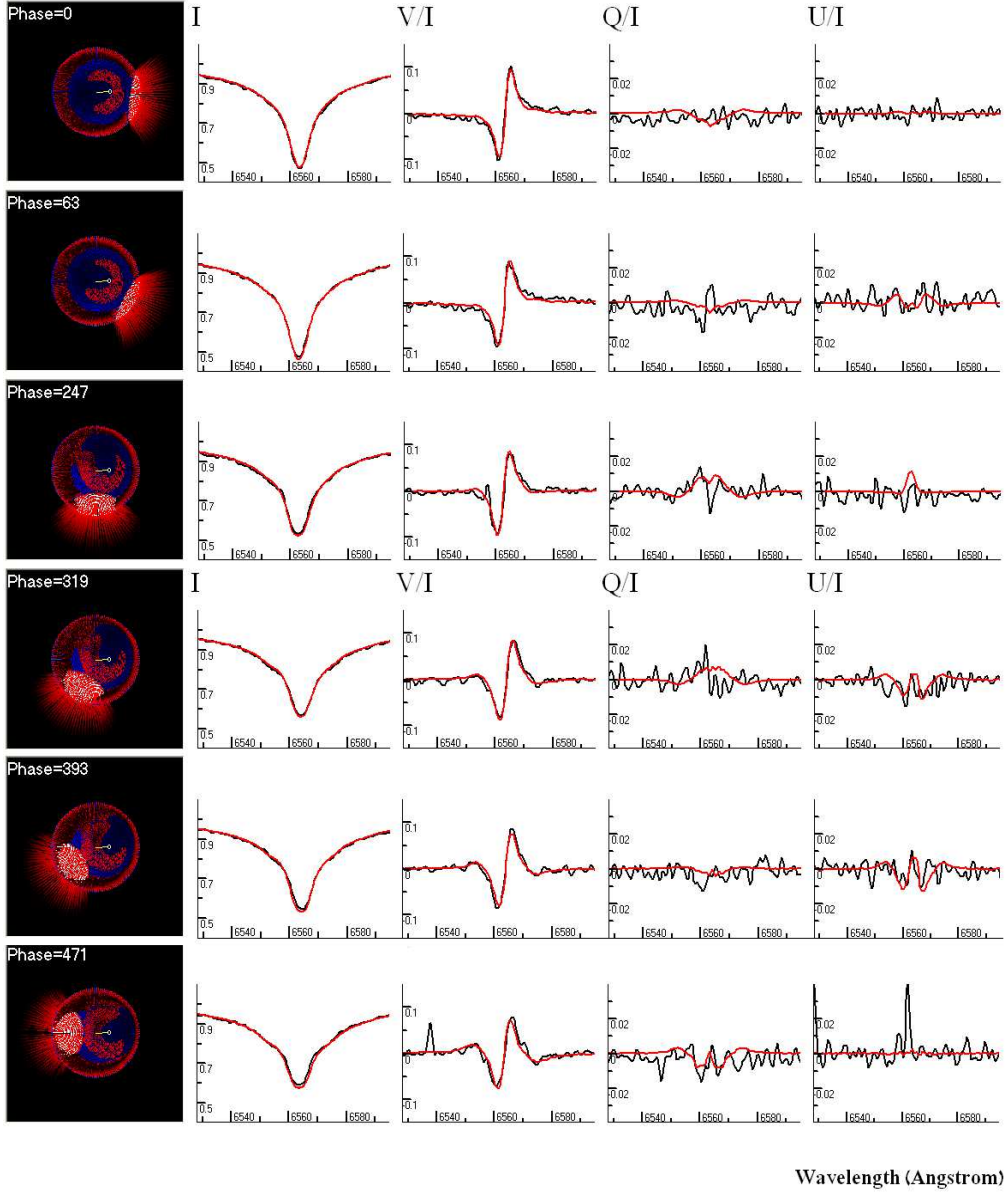


Fig. 11.— Model fits (red lines) of the observed (black lines) Stokes $IVQU$ spectra obtained in observations with the VLT. The corresponding tomographic portraits of the star’s magnetosphere and rotational phase (marked as **Phase**) are presented at left. The strong-field area is shown by white. The magnetic field line of force are red lines.

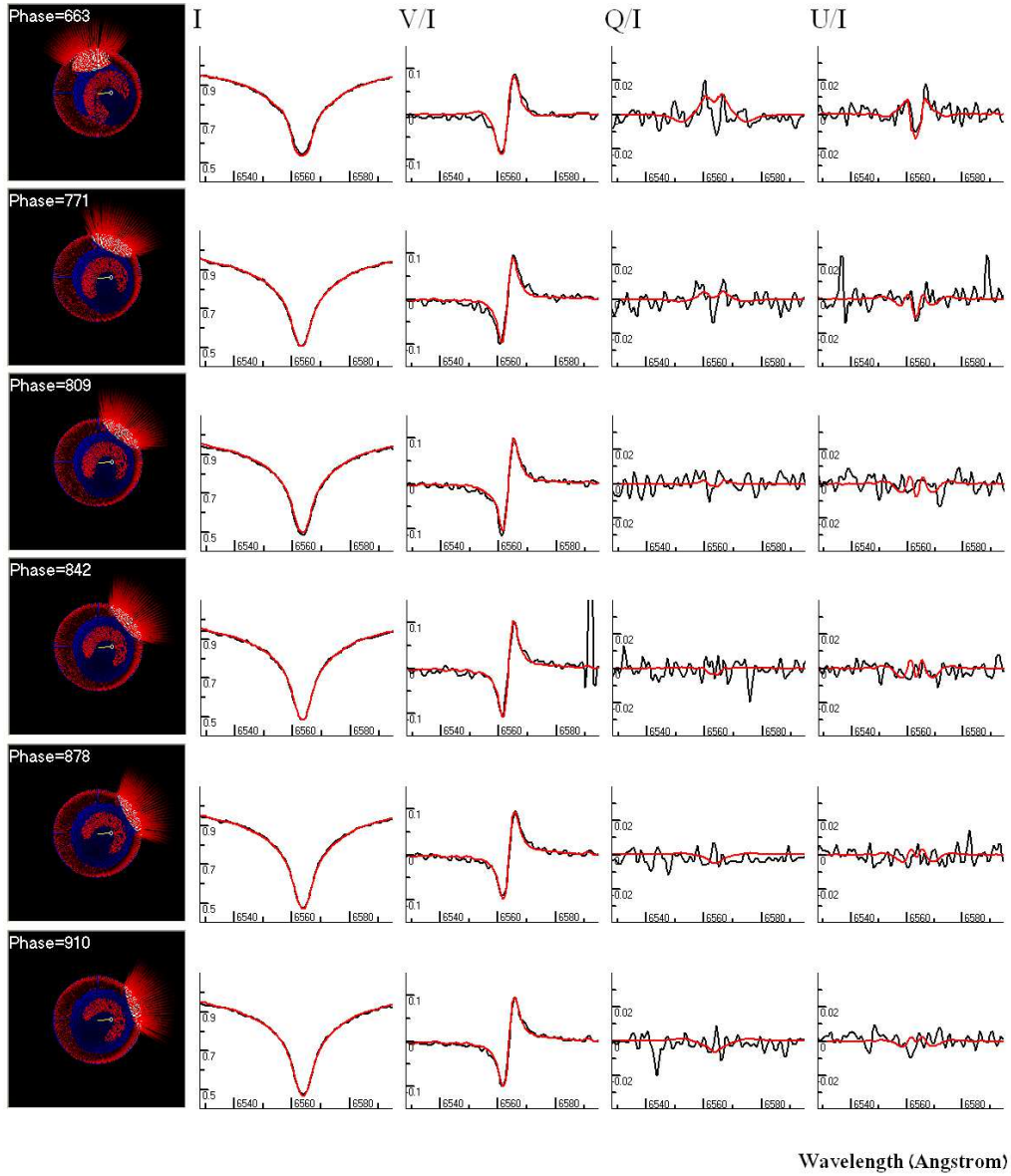


Fig. 12.— continued.